



# Rippled metamaterials with scale-dependent tailorable elasticity

Jian Zhou<sup>a,b,1</sup>, Richard Huang<sup>c,1</sup>, Nicolai Moldovan<sup>a</sup>, Liliana Stan<sup>a</sup>, Jianguo Wen<sup>a</sup>, Dafei Jin<sup>a,d</sup>, David R. Nelson<sup>c,2</sup>, Andrej Košmrlj<sup>e,f</sup>, David A. Czaplewski<sup>a</sup>, and Daniel López<sup>g</sup>

Affiliations are included on p. 6.

Contributed by David R. Nelson; received December 2, 2024; accepted February 11, 2025; reviewed by Aharon Kapitulnik and John A. Rogers

Thermally induced ripples are intrinsic features of nanometer-thick films, atomically thin materials, and cell membranes, significantly affecting their elastic properties. Despite decades of theoretical studies on the mechanics of suspended thermalized sheets, controversy still exists over the impact of these ripples, with conflicting predictions about whether elasticity is scale-dependent or scale-independent. Experimental progress has been hindered so far by the inability to have a platform capable of fully isolating and characterizing the effects of ripples. This knowledge gap limits the fundamental understanding of thin materials and their practical applications. Here, we show that thermal-like static ripples shape thin films into a class of metamaterials with scale-dependent, customizable elasticity. Utilizing a scalable semiconductor manufacturing process, we engineered nanometer-thick films with precisely controlled frozen random ripples, resembling snapshots of thermally fluctuating membranes. Resonant frequency measurements of rippled cantilevers reveal that random ripples effectively renormalize and enhance the average bending rigidity and sample-to-sample variations in a scale-dependent manner, consistent with recent theoretical estimations. The predictive power of the theoretical model, combined with the scalability of the fabrication process, was further exploited to create kirigami architectures with tailored bending rigidity and mechanical metamaterials with delayed buckling instability.

metamaterials | resonators | rippled materials

The mechanical properties of slender structures are well understood (1–3), and are routinely considered when designing safe transportation enclosures (e.g., containers, submarines, planes), stable buildings, flexible electronics, as well as metamaterials and kirigami architectures with unique mechanical properties (4–6). The effects of material properties, elastic deformations, and critical loads can be precisely predicted and engineered using scale-free elasticity theory (1, 3, 7). For example, introducing periodic corrugations is a common strategy that can be accurately modeled with thin-plate theory to enhance the bending rigidity of ultralight mechanical devices and flexible metamaterials, effectively delaying buckling (4, 8–10). However, as the characteristic dimensions of structures shrink to the nanoscale, ripples spontaneously form due to thermal fluctuations (11–13), rendering conventional thin-plate theory (1, 3, 7) inadequate for describing their elasticity (14–17).

Despite decades of research, the influence of the ripples on the mechanical properties of materials remains poorly understood and subject to ongoing controversy. Experiments on atomically thin devices have revealed that ripples induce substantial deviations from thin-plate theory, with mechanical properties varying by orders of magnitude across samples (17–19). Theoretical models have long suggested that thermal ripples impart scale-dependent elasticity to these materials (20–23), a hypothesis supported by atomistic and coarse-grained simulations (24–27). However, recent studies have questioned this view, proposing instead that bending rigidity remains scale-independent (28). Understanding these rippling effects is crucial to resolving this controversy and advancing the broader application of thin-film materials across various fields, where precise control over mechanical properties—and their interaction with electronic, thermal, optical, or chemical behaviors (29–31)—is vital. Yet, the challenge of quantifying the elastic effects induced by ripples persists due to the difficulties in isolating the coupling effects of dynamic ripples from built-in strain, static ripples, and defects (17–19, 32, 33), underscoring the need for further experimental and theoretical advances.

Here, we combine experiment and theory to demonstrate that thermal-like frozen ripples transform thin films into a class of metamaterials with scale-dependent, tailorable elasticity. We study the frequency responses of nanometer-thick  $Al_2O_3$  cantilevers with particular frozen random ripples, which resemble snapshots of thermally fluctuating

## Significance

Thermally induced ripples are intrinsic features of ultrathin sheets, including biological membranes and two-dimensional materials. Despite decades of research, their influence on elasticity remains debated, with predictions varying between strongly scale-dependent and scale-independent elastic parameters. Combining theoretical and experimental approaches, this work illuminates the long-standing controversy by demonstrating that random ripples in nanometer-thin materials renormalize and enhance bending rigidity in a scale-dependent manner. We observe not only a scale-dependent bending rigidity but also large sample-to-sample fluctuations, indicating a lack of self-averaging. By incorporating frozen thermal-like ripples into nanofilms, we create a class of disordered metamaterials with unique, scale-dependent, and customizable mechanical properties. These results deepen our understanding of rippled materials and open opportunities for designing devices with tailored elasticity.

The authors declare no competing interest.

Copyright © 2025 the Author(s). Published by PNAS. This open access article is distributed under [Creative Commons Attribution-NonCommercial-NoDerivatives License 4.0 \(CC BY-NC-ND\)](#).

<sup>1</sup>J.Z. and R.H. contributed equally to this work.

<sup>2</sup>To whom correspondence may be addressed. Email: drnelson@fas.harvard.edu.

This article contains supporting information online at <https://www.pnas.org/lookup/suppl/doi:10.1073/pnas.2425200122/-/DCSupplemental>.

Published March 19, 2025.

free-standing membranes at specific temperatures. Our experiments reveal that the rippled cantilevers exhibit enhanced and strongly size-dependent effective bending rigidity, with sample-to-sample variations that increase with the size of the films. This is in stark contrast to conventional elasticity theory (1–3), where macroscopic elastic parameters such as bending rigidity do not depend on the planar dimensions of the plate. The mechanical properties of these rippled nanobeams can be statistically described by considering the geometrically nonlinear coupling between different Fourier modes of the ripples. Furthermore, we have exploited these insights to design mechanical structures that exhibit unusual elastic responses.

Films of  $Al_2O_3$  with predetermined random height profiles, i.e., ripples, were fabricated using semiconductor nanofabrication processes through a conformal transfer technique (Fig. 1A and SI Appendix, Fig. S1). Silicon wafers were used as substrates to build cantilevers with and without frozen ripples. The polished side of the silicon wafer, known as the frontside, is smooth enough to enable the fabrication of microelectronics, micromechanical devices, microscopic robots, and more (34, 35). The backside of the wafer typically remains unpolished, with surface roughness determined by the wafer finishing process. While the backside of a wafer is avoided in conventional nanofabrication

processes, we exploit it in this study to conformally imprint its surface topography on nanometer-thick free-standing films (SI Appendix, Fig. S1C). Fig. 1A shows the procedure followed to fabricate both nanometer-thick smooth films and films with frozen random ripples with various in-plane dimensions. Amorphous films deposited by atomic layer deposition methods on the smooth side of a wafer result in atomically smooth films, while films deposited on the rough side of the wafer incorporate the random topography of the backside surface. Detailed fabrication and characterization processes are provided in *Materials and Methods*.

To characterize the roughness of a wafer surface with the disordered height profile  $h(\mathbf{x})$ , we measured the 2D power spectrum as  $P(\mathbf{q}) \equiv |h(\mathbf{q})|^2$ , where the Fourier components are given by  $h(\mathbf{q}) = \int d^2\mathbf{x} e^{-i\mathbf{q}\cdot\mathbf{x}} h(\mathbf{x})/A$ . The power spectra for both the smooth frontside and the rough backside wafer surfaces scale as  $P(\mathbf{q}) \sim q^{-4}$  at short lengthscales (large wavevector  $q$ ) albeit with very different numerical prefactors (Fig. 1B). The power-law dependence of the wafer surface profiles aligns with a widely observed scaling law found across various types of surfaces, including natural, synthetic, and machined surfaces (36, 37). Notably, free-standing membranes under thermal fluctuations also exhibit a power-law dependence with

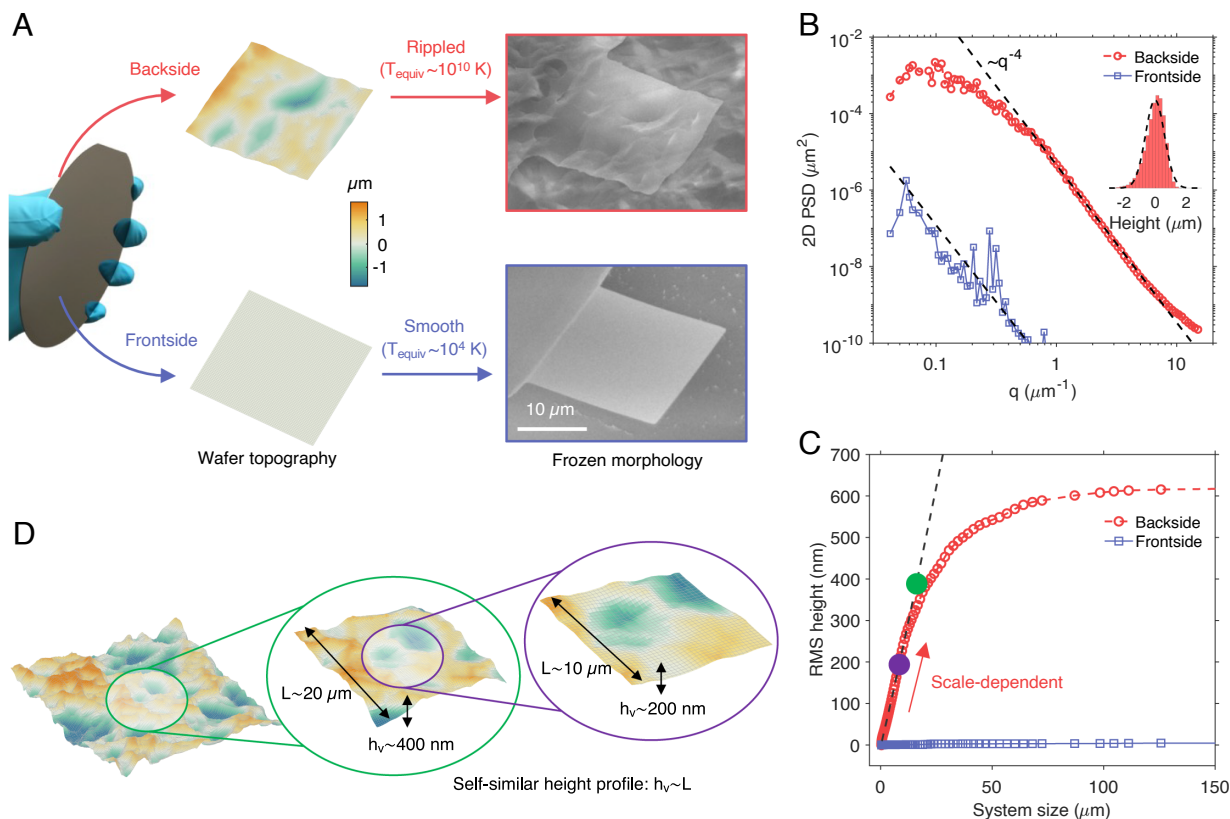


**Fig. 1.** Disordered membranes with thermal-like, frozen random ripples: conformal transfer fabrication and ripple characterization. (A) Conformal transfer fabrication of smooth and randomly rippled cantilevers. The polished surface of a Si wafer (frontside) is used to fabricate smooth resonators, and the unpolished side (backside) is used for the rippled ones (*Materials and Methods*). The color bar indicates the height profile  $h(x, y)$  of the wafer measured with a 3D surface profiler. The scanning electron micrographs show  $Al_2O_3$  cantilevers with a thickness  $t = 28$  nm that were fabricated on the frontside (smooth) and backside (rippled) of the Si wafer. The fabricated cantilevers resemble frozen snapshots of 28-nm thick membranes, thermally fluctuating at equivalent temperatures of  $T_{\text{equiv}} \sim 10^4$  K for smooth-surfaced cantilevers and  $T_{\text{equiv}} \sim 10^{10}$  K for rippled cantilevers. (B) Two-dimensional (2D) power spectral density (PSD) of the wafer surface height profile  $P(\mathbf{q}) \equiv |h(\mathbf{q})|^2$  measured over an area of  $284 \times 213 \mu\text{m}^2$ . Dashed lines correspond to the power spectrum of thermally fluctuating membranes ( $\langle |h(\mathbf{q})|^2 \rangle = k_B T / (A \kappa_0 q^4)$ ), where  $k_B$  is the Boltzmann constant,  $A$  the membrane area, and  $\kappa_0$  the bare membrane bending rigidity. Temperature in the spectrum of thermally fluctuating membranes was fitted to the 2D PSD of wafer surfaces to obtain the equivalent temperatures  $T_{\text{equiv}}$  as shown in (A). *Inset* figure shows the height distribution of the wafer backside rough surface, fitted to the Gaussian distribution. (C) Scale dependence of the rms height fluctuation  $h_v(L)$ , where  $L$  is the side length of a square membrane. The large solid dots correspond to the zoomed views in (D). The height fluctuations of rippled membranes are self-similar in the sense that  $h_v(L) \sim L$  (dashed line). (D) Visual depiction of the self-similar height profile.

an exponent of 4 (12, 38), consistent with the wafer surface profiles. As a result, the fabricated films, with geometry templated from the wafer surfaces, can be interpreted as frozen snapshots of thermally fluctuating free-standing membranes at specific temperatures. Note that changes in boundary conditions could influence the ripple characteristics and the effective mechanical properties of the membranes. Frozen analogs of thermal ripples can be produced not only in free-standing membranes but also in membranes with other boundary conditions, such as edge tension, provided that a rough surface with an appropriate power spectrum is templated (*SI Appendix, Text*).

Upon estimating the bare bending rigidity  $\kappa_0$  for a flat membrane as  $\kappa_0 = Et^3/[12(1 - \nu^2)]$  (39, 40), where  $E$ ,  $t$ ,  $\nu$  are three-dimensional (3D) Young's modulus, thickness, and 3D Poisson ratio respectively, an equivalent temperature for a thermally fluctuating membrane follows from the power spectrum of wafer surfaces were determined to be  $T_{\text{equiv}} \sim 10^4$  K for the smooth-surfaced films and  $T_{\text{equiv}} \sim 10^{10}$  K for the rippled films (Fig. 1B). Our approach enables the quantitative study of the rippling effect in a frozen state at extremely high equivalent temperatures, which would otherwise be unattainable. Since experiments were performed at much lower room temperatures ( $T \approx 300$  K), the amplitude of dynamic thermal ripples was much lower than the magnitude of imprinted static thermal-like ripples due to the wafer surface roughness. We also note that the rms of the height fluctuations

$$h_v(L) = \left[ \sum_{2\pi/L < q} |h(\mathbf{q})|^2 \right]^{1/2} \quad [1]$$

over a patch of size  $L \times L$  scales as  $h_v(L) \sim L$  up to a length scale of  $L \sim 20 \mu\text{m}$  (Fig. 1C). All fabricated rippled films fall within this range and thus they exhibit a self-similar profile with a constant ratio  $h_v(L)/L$  of the RMS height fluctuations to the patch size (Fig. 1D).

We determined the mechanical behavior of both smooth and rippled cantilevers by measuring their resonance frequencies at room temperature using a Fabry–Perot optical interferometer (*SI Appendix, Fig. S1*), specially designed for measuring the dynamics of nanometer-thick films (41). Fig. 2B shows the measured resonance frequency of multiple smooth and rippled cantilevers with the same thickness,  $t$ , and planar dimensions (length  $L$  and width  $W$ ). As expected, all the smooth cantilevers exhibit a similar resonance frequency with little sample-to-sample deviation, which can be precisely determined by the geometry of the structure using the thin-plate theory (1, 2). The rippled cantilevers exhibit a higher resonance frequency due to the introduction of ripples, but unlike the smooth structures, its value cannot be predicted using only the geometrical dimensions  $L$ ,  $W$ , and  $t$ . All the tested rippled cantilevers have the same geometrical dimensions and average random height profile, but their resonance frequencies are significantly different.

To investigate the dependence of mechanical properties on film size, we characterized the effective bending rigidity across hundreds of smooth and rippled cantilevers with varying dimensions (Fig. 2,  $L \geq W$ ). The resonance frequency  $f$  of a cantilever can be expressed as  $f = (1/2\pi)\sqrt{k_{\text{eff}}/m_{\text{eff}}}$ , where  $k_{\text{eff}} = 3\kappa_R W/L^3$  is the effective spring constant, and  $m_{\text{eff}} \approx 0.24\rho tLW$  is the effective mass at the cantilever tip (17, 42),  $\kappa_R$  is the effective bending rigidity, and  $\rho$  is the material density. From the measured resonance frequencies, the effective bending

rigidity,  $\kappa_R$ , of the smooth and rippled vibrating structures can be obtained.

As shown in Fig. 2 C–F, the effective bending rigidity of smooth beams is  $\kappa_R \approx \kappa_0$  for all the measured samples (blue squares) and is thus scale-independent. In contrast, the effective bending rigidity  $\kappa_R$  of rippled cantilevers shows a clear scale-dependent behavior (red circles): the larger the system dimensions, the larger the bending rigidity. The normalized measured effective bending rigidity  $\kappa_R/\kappa_0$  of rippled resonators, whose widths are smaller or equal to their lengths ( $L \geq W$ ), scales linearly with the width of the samples,  $\kappa_R/\kappa_0 \sim W$  (Fig. 2 C and E), remains independent of the length  $L$  (Fig. 2D), and is inversely proportional to the thickness of the films,  $\kappa_R/\kappa_0 \sim 1/t$  (Fig. 2F), approaching the classical thin-plate limit for large thicknesses. Fig. 2 also illustrates another striking property of the rippled cantilevers: There are scale-dependent sample-to-sample fluctuations in the effective bending rigidity that increase with the width of the films ( $L \geq W$ ), remain independent of the samples' length and get reduced when the thickness of the cantilevers increases (*SI Appendix, Fig. S2*). Therefore, rippled membranes present non-self-averaging behavior, similar to some other examples of disordered systems such as spin glasses (43) or disordered metals (44–46).

Previous theoretical analysis of membranes with quenched random ripples (47) demonstrated that the average effective bending rigidity,  $\bar{\kappa}_R(\ell)$ , of a square membrane of size  $\ell \times \ell$ , depends on the RMS height fluctuations  $h_v(\ell)$  of ripples. When the height fluctuations of the ripples are small compared to the film thickness ( $h_v(\ell) \ll t$ ), the effect of ripples is negligible, and the effective bending rigidity is well approximated with the classical thin-plate theory, i.e.,  $\bar{\kappa}_R(\ell) \approx \kappa_0$ . This is indeed the case for smooth cantilevers (Figs. 1C and 2 C–F). When the ripples are large compared to the film thickness ( $h_v(\ell) \gg t$ ), the ripples effectively renormalize and increase the bending rigidity to  $\bar{\kappa}_R(\ell)/\kappa_0 \sim h_v(\ell)/t$  due to the geometrically nonlinear coupling between different ripples' Fourier modes (*SI Appendix, Text*). For rectangular membranes with  $L > W$ , we can imagine the membrane as composed of a linear string of  $W \times W$  blocks, in which case, the width  $W$  sets the renormalization scale (48, 49). For rippled cantilevers in our experiments, the theory predicts that the average effective bending rigidity scales as

$$\frac{\bar{\kappa}_R(W)}{\kappa_0} \sim \frac{h_v(W)}{t} \sim \frac{W}{t}. \quad [2]$$

The above scaling for the average effective bending rigidity is consistent with the experimental measurements of rippled cantilevers in Fig. 2 C–F. As discussed above, the amplitude of dynamic thermal ripples is much smaller than the amplitude of static frozen ripples. Thus, the mechanical response is entirely dominated by the frozen thermal-like ripples. The observed scale-dependent elasticity represents disordered free-standing membranes where the thermal fluctuations are now quenched. It parallels the predicted scale-dependent properties of thermal ripples in flat membranes, with only a slight difference in the scaling exponents (23).

In *SI Appendix, Text*, we extend the theoretical analysis in ref. 47 to also predict the SD of the effective bending rigidity  $\Delta\kappa_R$ . It was found to scale as

$$\frac{\Delta\kappa_R(W)}{\kappa_0} \sim \frac{W}{t} \quad [3]$$

which is also in excellent agreement with the experimental measurements (*SI Appendix, Fig. S2*). For applications requiring

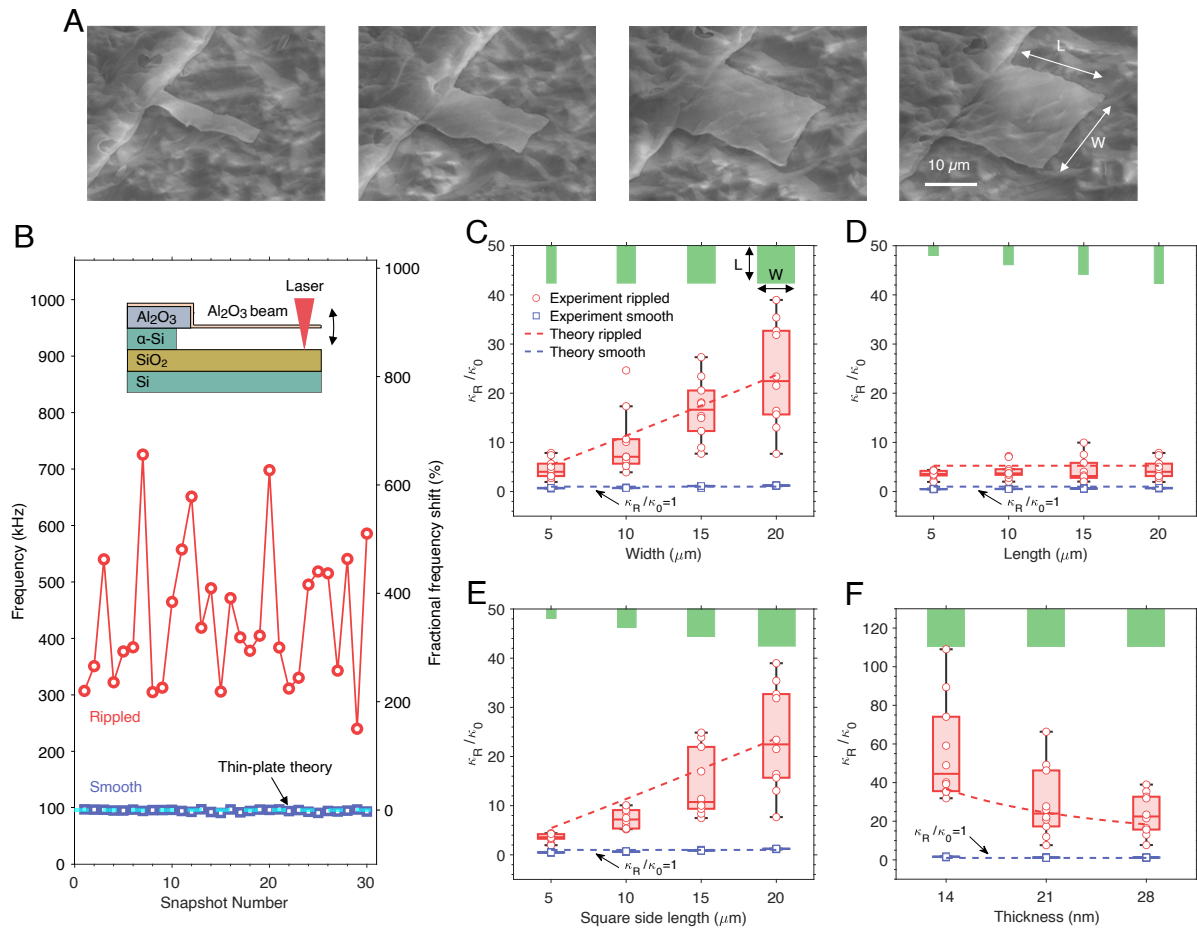


**Fig. 2.** Scale dependence of the effective bending rigidity of rippled cantilevers. (A) Scanning electron micrographs of rippled  $Al_2O_3$  cantilevers ( $L = 20 \mu m$ ,  $t = 28 nm$ ) with different widths. The resonators are fabricated on the same wafer to ensure they have a random height profile  $h(x,y)$  with the same statistical distribution. (B) Resonance frequency fluctuations were measured for 30 different rippled and smooth cantilevers with identical thickness ( $t = 28 nm$ ) and planar dimensions ( $L = W = 20 \mu m$ ), and compared to the prediction from the thin-plate theory (cyan dashed line). All resonance frequencies are measured with a custom-designed optical interferometer, excited by room temperature thermomechanical noise (*Materials and Methods*). (C–F) Effective bending rigidity  $\kappa_R$  of smooth and rippled cantilevers as a function of the sample dimensions: (C) variable width  $W$  ( $L = 20 \mu m$ ,  $t = 28 nm$ ), (D) variable length  $L$  ( $W = 5 \mu m$ ,  $t = 28 nm$ ), (E) variable side length  $L = W$  of square cantilevers ( $t = 28 nm$ ), and (F) variable thickness  $t$  ( $L = W = 20 \mu m$ ). The effective bending rigidity  $\kappa_R$  is obtained from the resonant frequency of the cantilever (see text) and compared to the bending rigidity  $\kappa_0 = Et^3/12(1-\nu^2)$  of flat films ( $\kappa_0 = 0.34 pJ$  for  $t = 28 nm$ -thick  $Al_2O_3$  films with the Young's modulus  $E = 180 GPa$  and Poisson's ratio  $\nu \approx 0.2$ ). The green insert in each figure shows the relative planar dimensions of cantilevers. Each box plot contains 10 samples of the same dimension, where the box encompasses 25th to 75th percentiles, the center line shows the median and whiskers extend to minimum and maximum values ( $\pm 2.7 SD$ ) not considering outliers. The dashed lines are the theoretical scaling predictions (see text).

high design reliability, sample-to-sample deviations caused by variations in rippling profiles can potentially be eliminated by using the same random rippled profile across all samples. Ignoring fabrication errors, imprinting the same random ripple patterns on different films would result in identical mechanical properties. Advanced 3D printing techniques (50), for instance, can be employed to precisely define and replicate the rippling profiles, thereby ensuring controlled and consistent mechanical behavior across various samples. Finally, note that the theory only predicts statistical properties of the bending rigidity by considering the statistical properties of an ensemble of power-law height fluctuations. The precise value of the effective bending rigidity for a given rippled cantilever depends on the detailed geometry of the ripples and can be estimated using Finite Element Analysis as shown in *SI Appendix, Fig. S3*.

Our findings provide a strategy for engineering slender structures with tailorable elasticity by capitalizing on the intrinsic mechanics of rippled films. The mechanical properties of rippled films can be programmed by the topography of the imprinted ripples and the local geometry of the structures. Using this strategy,

we have designed nanometers thick structures with mechanical responses unattainable when fabricated with smooth structural materials. In Fig. 3A, we show the evolution of the measured bending rigidity of square cantilevers ( $L = W = 20 \mu m$ ,  $t = 14 nm$ ), with and without cuts along the axial direction. The measured bending rigidity of rippled cantilevers shows a strong dependence on the number of cuts (red circles), while the smooth cantilevers remain insensitive to the presence of cuts (blue squares). This difference arises because the renormalization of the bending rigidity only occurs up to the width of individual strips as discussed above. Hence, under the same uniform bending stress, the out-of-plane bending angle of rippled cantilevers can be controlled by the number of axial cuts patterned during the fabrication process. We demonstrate this by patterning cantilevers of  $Al_2O_3$  ( $t = 28 nm$ ) with 1, 2, and 4 axial cuts and then deposit a 10 nm film of  $Ti$  on top. The metallic film introduces a uniform bending stress, causing the beams to bend upward (Fig. 3B) (51). The fabricated beams behave as predicted; see Fig. 3C: The higher the number of cuts, the larger the deflection angle. Smooth cantilevers exhibit upward bending

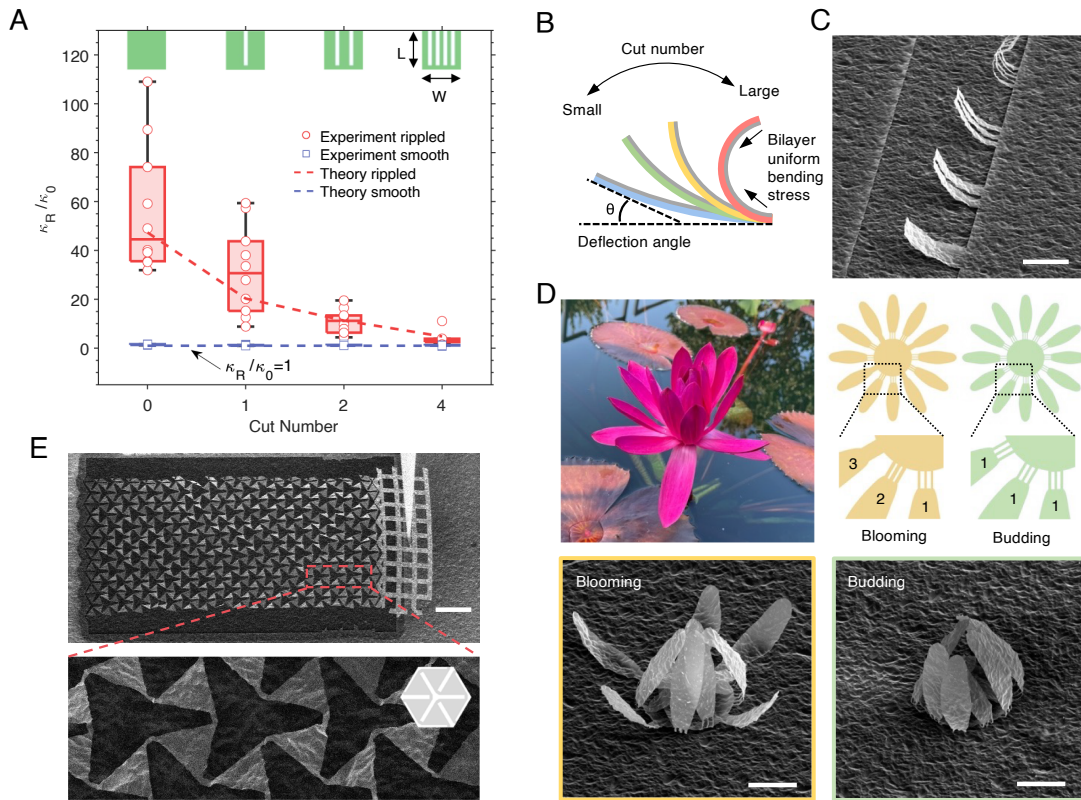


**Fig. 3.** Tailorable mechanical properties of rippled films through cutting. (A) Comparison of measured effective bending rigidity in smooth and rippled cantilevers with axial cuts, showcasing programmable bending rigidity via axial cuts. All square cantilevers have the same thickness ( $t = 14$  nm) and planar dimensions ( $L = W = 20$   $\mu$ m), with each cut being  $18$   $\mu$ m long and  $w_c = 2$   $\mu$ m wide. Since the renormalization of the bending rigidity in films with  $n$  cuts only occurs up to the width  $w_s(n) = (W - nw_c)/(n + 1)$  of individual strip, the average effective bending rigidity is expected to scale as  $\bar{\kappa}_R/\kappa_0 \sim w_s(n)/t$  (dashed red line). (B) Schematic depicting the expected bending responses of rippled beams under a uniform bending load as the number of cuts increases, illustrating the ability to program expected out-of-plane deformations via in-plane cuts. (C) SEM image of  $Al_2O_3$  rippled films ( $t = 28$  nm) with identical dimensions and an increasing number of cuts from 0 (Bottom) to 4 (Top). A 10 nm thick film of  $Ti$  is sputtered on top of the beams to induce a uniform bending load. (D) Fabrication of kirigami architectures with complex 3D shapes through the patterning of initial 2D planar geometries. This technique has been applied to create 3D rippled microstructures that emulate a Waterlily flower (*Nymphaea* "Red Flare"). SEM images show the resulting structures from different planar designs: budding and blooming architectures. Bending angle of flower petals is induced by the sputtering of a  $Ti$  film and controlled by the number of cuts in the hinges (see schematic designs). (E) Mechanical metamaterial constructed with rippled films. The SEM image shows a perforated rippled film with delayed buckling-induced deformation. The films have a thickness  $t = 28$  nm and an aspect ratio of  $L/t \approx 30,000$  (Movie S1). The lower SEM image shows a detail of the pattern of cuts defining the unit cell. (Scale bars in C and D, 50  $\mu$ m; scale bar in E, 100  $\mu$ m.)

with a constant deflection angle, independent of the number of cuts. Patterned rippled films thus enable programmable out-of-plane deformations via local geometrical control, providing a method to assemble origami and kirigami micro- and nanostructures (6, 52). This alternative method to assemble 3D structures is demonstrated in Fig. 3D, where the final 3D architecture of a micrometer size kirigami structure, inspired by a waterlily flower, is determined only by the dimensions of the cuts patterned onto the 2D rippled structure.

Using rippled films as a structural material with scale-dependent mechanical properties provides new degrees of freedom for engineering metamaterials with enhanced performance. Mechanical metamaterials have garnered significant attention in the past years because they exhibit negative Poisson's ratio (53), anomalous thermal expansion (54), and, under uniaxial tension, they experience out-of-plane buckling useful to build 3D kirigami architectures (6, 10, 55). Inspired by many functionally efficient but structurally disordered biological materials such as the hierarchical organization of trabecular bones and the cell organization of carnivorous plants, there has recently been increasing interest in studying disorder in metamaterials, aiming to provide better functionalities over ordered structures (56). The scale-dependent tailorable elasticity of rippled materials with

disorder can also be applied to the creation of metamaterials with delayed buckling. In Fig. 3E, a kirigami structure with a length-to-thickness ratio  $L/t \approx 30,000$  undergoes deformation via a uniaxial force applied with a nanoprobe. The structure, created by cuts on a rippled elastic thin sheet, features large triangular domains (scale length  $L_d$ ) connected by small rectangular hinges (scale length  $L_b$ ). Notably, the bending rigidity of the triangular domains is selectively enhanced over the hinges by a factor of  $L_d/L_b \approx 10$ , eliminating the need for adding thick stiffening elements to the triangular domains (57). Meanwhile, since the critical load in Euler buckling instability increases with the bending rigidity (27, 58, 59), structures built with rippled films, as shown in Fig. 3E, exhibit buckling at a significantly increased critical load. The out-of-plane buckling threshold strain for a rippled hinge is increased by a factor of  $(L_b/t)^2$  compared to a smooth hinge, and thus, the in-plane deformation regime is extended for rippled kirigami structures compared to smooth ones (SI Appendix, Text and Movie S1).

The results presented in this manuscript demonstrate that thin films with thermal-like frozen ripples have unique mechanical properties that cannot be described with the well-known Hookean thin-plate theory. These materials represent a class of metamaterials that exhibit enhanced bending rigidity,

strongly scale-dependent elastic parameters, and sample-to-sample variations proportional to the size of the structures. We introduced a theoretical model that describes the experimental results by taking into account the statistical properties of the height profile of the ripples and a nanofabrication approach that enables the manufacturing of structures and devices incorporating rippled materials. The predictive power of the theoretical model, combined with the scalability of the fabrication process, conveys a strategy for manufacturing complex micro- and nanostructures out of rippled films with tailorable elasticity.

## Materials and Methods

**Fabrication.** To fabricate rippled nanomembranes, we first deposit a layer of  $\text{SiO}_2$  film with 0.5  $\mu\text{m}$  thickness onto  $\text{Si}$  substrate with a rough surface (backside of the wafer) using plasma-enhanced chemical vapor deposition (PECVD). An amorphous silicon ( $a\text{-Si}$ ) film of 2.5  $\mu\text{m}$  thickness is then deposited using PECVD as the sacrificial layer for nanomembrane release. To avoid inconsistencies caused by differences in the characteristics of wafer surface profiles, which depend on the wafer finishing processes, all rippled samples were fabricated on a single wafer exhibiting consistent 2D power spectral density of height profiles across different locations (SI Appendix, Fig. S1B). To fabricate smooth nanomembranes, we use a commercially available SOI wafer with a 2.5  $\mu\text{m}$  device silicon layer and a 1  $\mu\text{m}$  buried oxide layer. A thick layer of atomic layer deposition (ALD)  $\text{Al}_2\text{O}_3$  (1,500 cycles) is deposited on both wafers as a supporting layer for the nanomembrane cantilevers. After patterning using optical lithography, the thick  $\text{Al}_2\text{O}_3$  film is dry etched approximately 3/4 of the way through the film using a  $\text{Cl}_2/\text{BCl}_3$  plasma and then wet etched in  $\text{H}_3\text{PO}_4$  solution the remaining way, stopping on the  $a\text{-Si}$  layer without roughening it. Following the etch, a thin layer of ALD  $\text{Al}_2\text{O}_3$  (nanomembrane structural layer) of the desired thickness is deposited. We use the same ALD processes for the thick and thin  $\text{Al}_2\text{O}_3$  films, except for the total number of cycles, where we use a trimethylaluminum (TMA) precursor and water as a reactant at 175  $^\circ\text{C}$ . After another lithography patterning, the thin layer of  $\text{Al}_2\text{O}_3$  film is etched in a  $\text{Cl}_2/\text{BCl}_3$  plasma. To fully release the  $\text{Al}_2\text{O}_3$  nanomembranes, we first remove the surrounding sacrificial layer near the nanostructures using  $\text{SF}_6$  reactive ion etching, then the sacrificial layer underneath the nanostructures is removed using  $\text{XeF}_2$  etching to avoid surface tension problems in a wet etch. The 3D structures are formed by sputtering a thin layer of Ti ( $t = 10$  nm) on the  $\text{Al}_2\text{O}_3$  nanomembranes ( $t = 28$  nm). For a cantilever under a uniform bending stress  $\sigma$ , the deflection at its tip  $V_{\text{max}} = \sigma L^4 / (8\kappa_R)$  (60). The bending stress can be estimated to be in the scale of 1 kPa from the deflection of rippled cantilevers, as shown in Fig. 3C.

**Characterization.** Cross-sectional scanning transmission electron microscopy (STEM) and X-ray reflectometry (XRR) are used to determine the film thickness of the  $\text{Al}_2\text{O}_3$  nanomembranes. SI Appendix, Fig. S1D shows the cross-sectional STEM image of a 28 nm-thick  $\text{Al}_2\text{O}_3$  nanofilm deposited on the front side of a wafer surface. STEM samples are prepared using focused ion beam (FIB) milling in a FEI Nova 600 NanoLab dual beam SEM/FIB. To protect the  $\text{Al}_2\text{O}_3$  film during cross-sectional sample preparation, a thin layer of Pt is first deposited onto the ALD film using electron beam (EB) deposition, followed by a thick layer of Pt deposited using focused ion beam (FIB) deposition (SI Appendix, Fig. S1D). Both STEM and XRR give similar growth rates of the ALD  $\text{Al}_2\text{O}_3$  nanofilm, about 1.08  $\text{\AA}$  per cycle. The density of the  $\text{Al}_2\text{O}_3$  nanofilm is estimated to be 3,300  $\text{kg}/\text{m}^3$  from the XRR measurement. Surface profiles are measured with a Keyence VK-X3000 3D surface profiler.

**Measurement.** The thermomechanical motion of the cantilevers is measured using a custom-made optical interferometry setup (41). The interference is

formed between the reflected light waves from the  $\text{Al}_2\text{O}_3$  nanomembrane and the underneath substrate as shown in SI Appendix, Fig. S1E. The light source is a polarized 632.8 nm HeNe laser with an incident power about 0.5 mW, detected by a photodetector (New Focus 1801 FS), and analyzed by a Lock-in amplifier (Zurich Instruments HF2LI). Devices are measured in a vacuum chamber with a pressure of  $<10^{-5}$  torr at room temperature. An example of the thermomechanical motion spectra of a smooth and a rippled nanomechanical resonator is provided in SI Appendix, Fig. S1F and G, respectively. The thermomechanical motion amplitudes are calibrated according to the equipartition theorem. While the rough surfaces have poorer reflection efficiency compared to the smooth surfaces, the interferometry setup has sufficient sensitivity to detect the thermomechanical motion of devices with rippling. The millimeter-scale elastic metamaterials are manipulated using an Omniprobe nanomanipulator. A Nova 600 NanoLab SEM records the motion.

**Finite Element Analysis.** Finite Element Analysis (FEA), as shown in SI Appendix, Fig. S3, was performed using commercial software to estimate the eigenfrequencies of the samples under small linear deformation, considering that our nanomechanical resonators are driven solely by thermomechanical motion. The FEA samples were created using the measured surface profiles from the 3D surface profiler (Keyence VK-X3000). The measurement was performed on the same wafer used to fabricate the experimental cantilever samples shown in Fig. 2. Each FEA device, with the desired planar dimensions (length and width), was randomly sampled from the measured surface profiles ( $x, y, z$ ) over an area of  $284 \times 213 \mu\text{m}^2$ , as shown in SI Appendix, Fig. S3A. The selected data were then converted into an STL file to facilitate geometry importing into the FEA software. The device thickness was assigned to match that of the experimental samples, and material properties, including a Young's modulus of 180 GPa and a density of 3,300  $\text{kg}/\text{m}^3$ , were applied based on experimental characterization. One end of the device was fixed to replicate the cantilever configuration. We observed that the fundamental mode of all FEA samples corresponds to out-of-plane vibration, which was used to estimate the bending rigidity.

**Data, Materials, and Software Availability.** All study data are included in the article and/or supporting information.

**ACKNOWLEDGMENTS.** D.R.N. and D.L. benefited from discussions with Mark Bowick at the early stages of this investigation. This work was performed at the Center for Nanoscale Materials, a U.S. Department of Energy Office of Science User Facility, and supported by the U.S. Department of Energy, Office of Science, under Contract No. DE-AC02-06CH11357. Work by R.H. and D.R.N. supported in part by the NSF, through the Harvard University Materials Research Science and Engineering Center, grant No. DMR-2011754. J.Z. acknowledges support from the NSF under Award No. ECCS-2428731 and startup funding from State University of New York Binghamton. D.J. acknowledges support from the NSF under Award Nos. CMMI-2037563 and CMMI-2314687. The work also received support from the NSF through the Career Award DMR-1752100 (A.K.).

Author affiliations: <sup>a</sup>Center for Nanoscale Materials, Argonne National Laboratory, Argonne, IL 60439; <sup>b</sup>Department of Mechanical Engineering, State University of New York at Binghamton, Binghamton, NY 13902; <sup>c</sup>Department of Physics, Harvard University, Cambridge, MA 02138; <sup>d</sup>Department of Physics and Astronomy, University of Notre Dame, Notre Dame, IN 46556; <sup>e</sup>Department of Mechanical and Aerospace Engineering, Princeton University, Princeton, NJ 08544; <sup>f</sup>Princeton Materials Institute, Princeton University, Princeton, NJ 08544; and <sup>g</sup>Materials Research Institute, Penn State University, University Park, PA 16802

Author contributions: J.Z., R.H., D.R.N., A.K., and D.L. designed research; J.Z., R.H., N.M., L.S., D.R.N., A.K., D.A.C., and D.L. performed research; J.Z., R.H., J.W., D.J., D.R.N., A.K., D.A.C., and D.L. analyzed data; and J.Z., R.H., D.R.N., A.K., D.A.C., and D.L. wrote the paper.

Reviewers: A.K., Stanford University; and J.A.R., Northwestern University-Evanston.

1. L. D. Landau, E. M. Lifshitz, A. M. Kosevich, L. P. Pitaevskii, *Theory of Elasticity* (Elsevier, 1986), vol. 7.
2. S. P. Timoshenko, *History of Strength of Materials* (McGraw-Hill, New York, 1953).
3. V. V. Novozhilov, *The Theory of Thin Shells* (P. Noordhoff, 1959).
4. K. Bertoldi, V. Vitelli, J. Christensen, M. Van Hecke, Flexible mechanical metamaterials. *Nat. Rev. Mater.* **2**, 1–11 (2017).
5. L. R. Meza et al., Resilient 3D hierarchical architected metamaterials. *Proc. Natl. Acad. Sci. U.S.A.* **112**, 11502–11507 (2015).
6. X. Zhang et al., Kirigami engineering-nanoscale structures exhibiting a range of controllable 3D configurations. *Adv. Mater.* **33**, 2005275 (2021).
7. S. Timoshenko et al., *Theory of Plates and Shells* (McGraw-hill New York, 1959), vol. 2.
8. C. R. Calladine, *Theory of Shell Structures* (Cambridge University Press, 1983).

9. K. Davami *et al.*, Ultralight shape-recovering plate mechanical metamaterials. *Nat. Commun.* **6**, 10019 (2015).
10. Y. Zhang *et al.*, A mechanically driven form of kirigami as a route to 3D mesostructures in micro/nanomembranes. *Proc. Natl. Acad. Sci. U.S.A.* **112**, 11757–11764 (2015).
11. J. C. Meyer *et al.*, The structure of suspended graphene sheets. *Nature* **446**, 60–63 (2007).
12. C. F. Schmidt *et al.*, Existence of a flat phase in red cell membrane skeletons. *Science* **259**, 952–955 (1993).
13. M. I. Katsnelson, Graphene: Carbon in two dimensions. *Mater. Today* **10**, 20–27 (2007).
14. D. R. Nelson, T. Piran, S. Weinberg, Eds., *Statistical Mechanics of Membranes and Surfaces* (World Scientific, Singapore, ed. 2, 2004).
15. B. Amorim *et al.*, Novel effects of strains in graphene and other two dimensional materials. *Phys. Rep.* **617**, 1–54 (2016).
16. P. Le Doussal, L. Radzihovsky, Anomalous elasticity, fluctuations and disorder in elastic membranes. *Ann. Phys.* **392**, 340–410 (2018).
17. M. K. Bles *et al.*, Graphene kirigami. *Nature* **524**, 204–207 (2015).
18. R. J. Nicholl *et al.*, The effect of intrinsic crumpling on the mechanics of free-standing graphene. *Nat. Commun.* **6**, 1–7 (2015).
19. G. Lopez-Polin *et al.*, Increasing the elastic modulus of graphene by controlled defect creation. *Nat. Phys.* **11**, 26–31 (2015).
20. D. R. Nelson, L. Peliti, Fluctuations in membranes with crystalline and hexatic order. *J. Phys.* **48**, 1085 (1987).
21. J. A. Aronovitz, T. C. Lubensky, Fluctuations of solid membranes. *Phys. Rev. Lett.* **60**, 2634–2637 (1988).
22. E. Gutter, F. David, S. Leibler, L. Peliti, Crumpling and buckling transitions in polymerized membranes. *Phys. Rev. Lett.* **61**, 2949 (1988).
23. A. Košmrlj, D. R. Nelson, Thermal excitations of warped membranes. *Phys. Rev. E* **89**, 022126 (2014).
24. M. J. Bowick, S. M. Catterall, M. Falcioni, G. Thorleifsson, K. N. Anagnostopoulos, The flat phase of crystalline membranes. *J. Phys.* **16**, 1321–1345 (1996).
25. A. Tröster, Fourier Monte Carlo renormalization-group approach to crystalline membranes. *Phys. Rev. E* **91**, 022132 (2015).
26. J. H. Los, A. Fasolino, M. I. Katsnelson, Scaling behavior and strain dependence of in-plane elastic properties of graphene. *Phys. Rev. Lett.* **116**, 015901 (2016).
27. A. Morshedifard, M. Ruiz-Garcia, M. J. A. Qomi, A. Košmrlj, Buckling of thermalized elastic sheets. *J. Mech. Phys. Solids* **149**, 104296 (2021).
28. U. Aseginolaza *et al.*, Bending rigidity, sound propagation and ripples in flat graphene. *Nat. Phys.* **20**, 1288–1293 (2024).
29. J. Martin *et al.*, Observation of electron-hole puddles in graphene using a scanning single-electron transistor. *Nat. Phys.* **4**, 144–148 (2008).
30. J. Zang *et al.*, Multifunctionality and control of the crumpling and unfolding of large-area graphene. *Nat. Mater.* **12**, 321–325 (2013).
31. D. W. Boukhvalov, M. I. Katsnelson, Enhancement of chemical activity in corrugated graphene. *J. Phys. Chem. C* **113**, 14176–14178 (2009).
32. R. J. Nicholl, N. V. Lavrik, I. Vlassioug, B. R. Srijanto, K. I. Bolotin, Hidden area and mechanical nonlinearities in freestanding graphene. *Phys. Rev. Lett.* **118**, 266101 (2017).
33. H. I. Rasool, C. Ophus, A. Zettl, Atomic defects in two dimensional materials. *Adv. Mater.* **27**, 5771–5777 (2015).
34. S. A. Campbell, *The Science and Engineering of Microelectronic Fabrication* (Oxford University Press, USA, 1996).
35. M. Z. Miskin *et al.*, Electronically integrated, mass-manufactured, microscopic robots. *Nature* **584**, 557–561 (2020).
36. A. L. Barabási, H. E. Stanley, *Fractal Concepts in Surface Growth* (Cambridge University Press, 1995).
37. T. D. Jacobs, T. Junge, L. Pastewka, Quantitative characterization of surface topography using spectral analysis. *Surf. Topogr. Metrol. Prop.* **5**, 013001 (2017).
38. A. Fasolino, J. Los, M. I. Katsnelson, Intrinsic ripples in graphene. *Nat. Mater.* **6**, 858–861 (2007).
39. S. D. Senturia, *Microsystem Design* (Springer Science & Business Media, 2005).
40. W. Weaver Jr., S. P. Timoshenko, D. H. Young, *Vibration Problems in Engineering* (John Wiley & Sons, 1991).
41. J. Zhou *et al.*, Approaching the strain-free limit in ultrathin nanomechanical resonators. *Nano Lett.* **20**, 5693–5698 (2020).
42. M. I. Younis, *MEMS Linear and Nonlinear Statics and Dynamics* (Springer Science & Business Media, 2011), vol. 20.
43. S. Wiseman, E. Domany, Finite-size scaling and lack of self-averaging in critical disordered systems. *Phys. Rev. Lett.* **81**, 22 (1998).
44. B. Altshuler, Fluctuations in the extrinsic conductivity of disordered conductors. *JETP Lett.* **41**, 648–651 (1985).
45. P. A. Lee, A. D. Stone, Universal conductance fluctuations in metals. *Phys. Rev. Lett.* **55**, 1622 (1985).
46. P. Lee, A. D. Stone, H. Fukuyama, Universal conductance fluctuations in metals: Effects of finite temperature, interactions, and magnetic field. *Phys. Rev. B* **35**, 1039 (1987).
47. A. Košmrlj, D. R. Nelson, Mechanical properties of warped membranes. *Phys. Rev. E* **88**, 012136 (2013).
48. A. Košmrlj, D. R. Nelson, Response of thermalized ribbons to pulling and bending. *Phys. Rev. B* **93**, 125431 (2016).
49. M. J. Bowick, A. Košmrlj, D. R. Nelson, R. Sknepnek, Non-hookean statistical mechanics of clamped graphene ribbons. *Phys. Rev. B* **95**, 104109 (2017).
50. L. R. Meza, S. Das, J. R. Greer, Strong, lightweight, and recoverable three-dimensional ceramic nanolattices. *Science* **345**, 1322–1326 (2014).
51. H. Windischmann, Intrinsic stress in sputter-deposited thin films. *Crit. Rev. Solid State Mater. Sci.* **17**, 547–596 (1992).
52. Y. Zhang *et al.*, Printing, folding and assembly methods for forming 3D mesostructures in advanced materials. *Nat. Rev. Mater.* **2**, 1–17 (2017).
53. S. Shan, S. H. Kang, Z. Zhao, L. Fang, K. Bertoldi, Design of planar isotropic negative poisson's ratio structures. *Extreme Mech. Lett.* **4**, 96–102 (2015).
54. P. Z. Hanakata, A. Plummer, D. R. Nelson, Anomalous thermal expansion in Ising-like puckered sheets. *Phys. Rev. Lett.* **128**, 075902 (2022).
55. A. Rafsanjani, K. Bertoldi, Buckling-induced kirigami. *Phys. Rev. Lett.* **118**, 084301 (2017).
56. M. Zaiser, S. Zapperi, Disordered mechanical metamaterials. *Nat. Rev. Phys.* **5**, 679–688 (2023).
57. K. J. Dorsey *et al.*, Atomic layer deposition for membranes, metamaterials, and mechanisms. *Adv. Mater.* **31**, 1901944 (2019).
58. A. Van der Heijden, *W. T. Koiter's Elastic Stability of Solids and Structures* (Cambridge University Press, New York, 2009).
59. D. Vella, Buffering by buckling as a route to elastic deformation. *Nat. Rev. Phys.* **1**, 425–436 (2019).
60. W. C. Young *et al.*, *Roark's Formulas for Stress and Strain* (McGraw-hill New York, 2002), vol. 7.

# PNAS



## Supporting Information for

### Rippled metamaterials with scale-dependent tailorable elasticity

Jian Zhou, Richard Huang, Nicolaie Moldovan, Liliana Stan, Jianguo Wen, Dafei Jin, David R. Nelson, Andrej Košmrlj, David A. Czaplewski, Daniel López

Corresponding Author: David R. Nelson (drnelson@fas.harvard.edu )

#### This PDF file includes:

- Supporting text
- Figs. S1 to S3
- Legend for Movie S1
- SI References

#### Other supporting materials for this manuscript include the following:

- Movie S1



## Supporting Information Text

### 1. Theoretical model for rippled membranes

The mechanical properties of rippled cantilevers at zero temperature can be understood theoretically by first writing the shallow-shell equilibrium equations for nearly flat membranes with quenched random disorder, as developed in Refs. (1, 2). We begin by briefly reviewing some of these results, summarizing the model in Section 1 and the scaling of the average effective bending rigidity in Section 2. In Section 3, we then discuss how the previous analysis can be extended to understand the scaling of sample-to-sample fluctuations in the effective bending rigidity. In Section 4, we discuss how ripples affect the buckling threshold in sheets and use this result to comment on the buckling of kirigami structures discussed in the main text. Section 5 summarizes how we estimated the effective temperatures that generate height fluctuations similar to the ripples in the experimental samples.

The reference unstressed configuration of a disordered, nearly flat membrane can be written in the Monge representation as

$$\mathbf{X}^0(\mathbf{x}) = x\hat{\mathbf{e}}_x + y\hat{\mathbf{e}}_y + h(\mathbf{x})\hat{\mathbf{e}}_z, \quad [1]$$

where  $h(\mathbf{x})$  represents a random height profile and  $\mathbf{x} \equiv (x, y)$ . In Fourier space, the height profile is given by  $h(\mathbf{q}) = \frac{1}{A} \int d^2\mathbf{x} e^{-i\mathbf{q}\cdot\mathbf{x}} h(\mathbf{x})$ , where  $A$  is the area of the membrane. Each Fourier mode  $h(\mathbf{q})$  is assumed to be an independent Gaussian random variable with zero mean  $\langle h(\mathbf{q}) \rangle = 0$  and variance

$$\langle h(\mathbf{q}_1)h(\mathbf{q}_2) \rangle = \delta_{\mathbf{q}_1, -\mathbf{q}_2} \frac{\Delta^2}{Aq_1^{d_h}}, \quad [2]$$

where  $\delta$  is the Kronecker delta and  $q \equiv |\mathbf{q}|$ . For the  $Al_2O_3$  rippled cantilevers considered in this paper, the measured two-dimensional power spectral density of the height profile in Figure 1b in the main text implies the exponent  $d_h = 4$ . The value of  $d_h = 4$  is inspired by thermal ripples in free-standing membranes given approximately by

$$\langle |h(\mathbf{q})|^2 \rangle \approx \frac{k_B T}{A\kappa_0 q^4}. \quad [3]$$

Although not the subject of the paper, note that other values of  $d_h$  could perhaps be of interest: for example, thermal ripples in membranes subject to an edge tension  $\sigma$  are instead

$$\langle |h(\mathbf{q})|^2 \rangle \approx \frac{k_B T}{A(\kappa_0 q^4 + \sigma q^2)}, \quad [4]$$

which corresponds to  $d_h \approx 2$  for suitably large systems. A change in  $d_h$  leads to different mechanical properties: for example, the effective bending rigidity will scale only logarithmically with system size for  $d_h = 2$ , as opposed to linearly for  $d_h = 4$ , see Ref. (1) for additional discussion.

One theoretical approach towards obtaining the effective bending rigidity of rippled membranes is to consider the mechanical response to a normal force density  $p(\mathbf{x})$  acting on the membrane. The resulting deformation can be decomposed into tangential displacements  $u_i(\mathbf{x})$  with  $i \in \{x, y\}$  and normal displacements  $f(\mathbf{x})$ , such that the deformed configuration  $\mathbf{X}(\mathbf{x})$  is

$$\mathbf{X} = \mathbf{X}^0 + u_i \hat{\mathbf{t}}_i^0 + f \hat{\mathbf{n}}^0, \quad [5]$$

where the summation over repeated indices is implied and we introduced the unit tangent vectors  $\hat{\mathbf{t}}_i^0 = (\hat{\mathbf{e}}_i + (\partial_i h)\hat{\mathbf{e}}_z) / \sqrt{1 + (\partial_i h)^2}$  and the unit normal vector and  $\hat{\mathbf{n}}^0 = (\hat{\mathbf{e}}_z - (\partial_i h)\hat{\mathbf{e}}_i) / \sqrt{1 + \sum_i (\partial_i h)^2}$ . The elastic free energy density  $\mathcal{F}$  of the deformed configuration is then

$$\mathcal{F} = \frac{1}{2} \lambda_0 u_{kk}^2 + \mu_0 u_{ij}^2 + \frac{1}{2} \kappa_0 K_{kk}^2 - \kappa_G^0 \det(K_{ij}), \quad [6]$$

where  $\lambda_0$  and  $\mu_0$  are the in-plane Lamé constant and  $\kappa_0$  and  $\kappa_G^0$  are the two-dimensional bending rigidity and the Gaussian bending rigidity, respectively. In the above Eq. (6) we also introduced the strain tensor  $u_{ij}(\mathbf{x})$  and the bending strain tensor  $K_{ij}(\mathbf{x})$  which can be expressed in terms of the tangential and normal displacements as

$$\begin{aligned} u_{ij} &= \frac{1}{2} (\partial_i u_j + \partial_j u_i) + \frac{1}{2} (\partial_i f)(\partial_j f) - f \partial_i \partial_j h, \\ K_{ij} &= \partial_i \partial_j f, \end{aligned} \quad [7]$$

where we kept only the lowest order terms. The equations describing the deformed configuration of the membrane in response to the applied normal force density  $p(\mathbf{x})$  can be obtained using the principle of virtual work, where we minimize the functional

$$F[u_i(\mathbf{x}), f(\mathbf{x})] = \int d^2\mathbf{x} (\mathcal{F} - pf). \quad [8]$$

For simplicity, we do not consider boundary forces or torques. Minimizing the functional in Eq. (8) leads to the shallow shell equilibrium equations

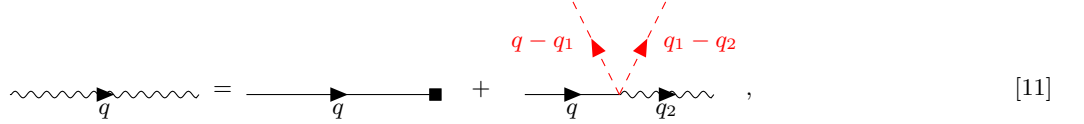
$$\begin{aligned} 0 &= \Delta^2 \chi + Y_0 \left[ \{h, f\} + \frac{1}{2} \{f, f\} \right], \\ p &= \kappa_0 \Delta^2 f - \{\chi, f\} - \{\chi, h\}, \end{aligned} \quad [9]$$

where  $Y_0 = 4\mu_0(\mu_0 + \lambda_0)/(2\mu_0 + \lambda_0)$  is the two dimensional Young's modulus and  $\Delta$  the Laplacian operator, and the Airy stress function  $\chi$  is related to the stress tensor  $\sigma_{ij} = \lambda_0 u_{kk} \delta_{ij} + 2\mu_0 u_{ij}$  via  $\sigma_{ij} = \epsilon_{ik} \epsilon_{jl} \partial_k \partial_l \chi$ . Here,  $\epsilon_{ij}$  is the Levi-Civita symbol in two dimensions. In the above Eq. (9) we also introduced the Airy bracket  $\{A, B\} = \epsilon_{ik} \epsilon_{jl} (\partial_i \partial_j A) (\partial_k \partial_l B)$ .

Once we specify  $d_h$ , the scaling of the effective bending rigidity of rippled membranes with the characteristic dimensions is not expected to be affected by a particular choice of boundary conditions, and we adopt periodic boundary conditions for convenience. Here, we consider the linear response to the applied normal force density  $p(\mathbf{q})$ . Thus we can omit the non-linear terms  $\{f, f\}$  and  $\{\chi, f\}$  in the shallow-shell equilibrium equations in Eq. (9) and solve for the normal displacements  $f(\mathbf{q})$ . This gives the self-consistent integral equation

$$f(\mathbf{q}) = \frac{p(\mathbf{q})}{\kappa_0 q^4} - \frac{Y_0}{\kappa_0 q^4} \sum_{\mathbf{q}_1, \mathbf{q}_2 \neq 0} \frac{(\mathbf{q} \times \mathbf{q}_1)^2 (\mathbf{q}_1 \times \mathbf{q}_2)^2}{q_1^4} h(\mathbf{q} - \mathbf{q}_1) h(\mathbf{q}_1 - \mathbf{q}_2) f(\mathbf{q}_2). \quad [10]$$

The above integral equation for normal displacements  $f(\mathbf{q})$  cannot be solved analytically for a given random profile  $h(\mathbf{q})$  of rippled membranes. Below we discuss, how we can approximately obtain statistical properties of the normal displacements  $f(\mathbf{q})$  using diagrammatic techniques. Diagrammatically, the integral equation in Eq. (10) can be represented as



$$\text{wavy line } q = \text{solid line } q \text{ with square vertex} + \text{solid line } q \text{ with red dotted lines } q_1 - q_2 \text{ and } q_1 - q_2, \quad [11]$$

where the wavy line represents the normal displacements  $f(\mathbf{q})$ , the solid line represents the propagator  $\frac{1}{\kappa_0 q^4}$ , the square vertex represents the applied normal force  $p(\mathbf{q})$ , and the red dotted lines represent the disordered profile  $h(\mathbf{q})$ . By iterating the integral equation in Eq. (10) or equivalently the diagrammatic equation in Eq. (11), one can obtain an infinite series of diagrams (as well as their analytical expressions) that contribute to the response  $f(\mathbf{q})$ .

## 2. Average effective bending rigidity

The average effective bending rigidity can be obtained from the linear response theory. In this section, we briefly summarize the results from Ref. (1). For a flat sheet without the quenched random disorder ( $h(\mathbf{q}) \equiv 0$ ), Eq. (10) simply gives  $f(\mathbf{q}) = p(\mathbf{q})/(\kappa_0 q^4)$ . The applied normal force density  $p(\mathbf{q})$  at a given Fourier mode  $\mathbf{q}$  thus induces the response of the same mode  $f(\mathbf{q})$ . However, for rippled membranes ( $h(\mathbf{q}) \neq 0$ ), the applied normal force density  $p(\mathbf{q})$  also induces the response  $f(\mathbf{q}')$  with  $\mathbf{q}' \neq \mathbf{q}$  due to the mode coupling in the second term in Eq. (10). Nevertheless, only one mode  $\mathbf{q}$  is induced in the average response  $\langle f(\mathbf{q}) \rangle$ , where the averaging is done over an ensemble of disordered rippled membranes with random height profiles  $h(\mathbf{q})$  with the zero mean and the variance in Eq. (2). In analogy with the above result for the flat sheet, we define the effective bending rigidity  $\kappa_R(q)$  via the average linear response

$$\langle f(\mathbf{q}) \rangle = \frac{p(\mathbf{q})}{\kappa_R(q) q^4}. \quad [12]$$

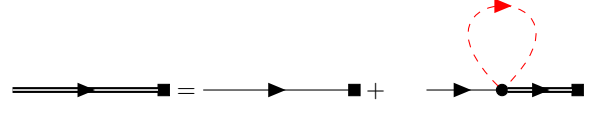
Diagrammatically, averaging over random height profiles of rippled membranes corresponds to contracting the red lines that arise in an infinite series of diagrams by iterating the Eq. (11). Note that the red lines have to be contracted in all possible ways according to the Wick's theorem.

Before summarizing the results for the average effective bending rigidity, it is useful to introduce the root-mean-square (RMS) height fluctuation  $h_v(q)$  over a patch of size  $2\pi/q \times 2\pi/q$  of the rippled membrane. It is given by

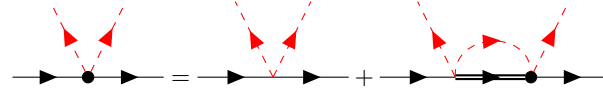
$$h_v^2(q) = \sum_{q < |\mathbf{k}| < \Lambda} \langle |h(\mathbf{k})|^2 \rangle \sim \begin{cases} \Delta^2 / q^{d_h - 2}, & d_h > 2 \\ \Delta^2 \ln(\Lambda/q), & d_h = 2, \\ \Delta^2 \Lambda^{2 - d_h}, & d_h < 2 \end{cases} \quad [13]$$

where  $\Lambda \sim 1/a$  is an UV cutoff set by a microscopic length scale  $a$ . Upon using iterative perturbation theory on Eq. (10), it was found that  $\langle f(\mathbf{q}) \rangle$  could be expressed as a perturbative series in the parameter  $Y h_v^2(q)/\kappa$ . For a membrane of thickness  $t$ , the two-dimensional Young's modulus and bending rigidity scale as  $Y \sim t$  and  $\kappa \sim t^3$ , respectively. Therefore, the perturbative parameter is related to the ratio of the effective height fluctuations and intrinsic thickness  $h_v(q)/t$ . The perturbation series converges for nearly flat membranes with  $h_v(q)/t \ll 1$  but it diverges for highly rippled membranes with  $h_v(q)/t \gg 1$ , which is the case at long wavelengths for the experimental  $Al_2O_3$  rippled membranes with  $d_h = 4$  considered in this paper.

In order to estimate the scaling properties of the divergent perturbation series, we used the Self-Consistent Screening Approximation (SCSA) where one sums the infinite subset of all diagrams. The SCSA was originally used to estimate critical exponents in critical phenomena (3, 4), and was later also used to estimate the scaling of effective elastic constants for thermally fluctuating membranes (5–7) and membranes with quenched random disorder (8, 9). From a more theoretical perspective, for a two dimensional membrane embedded in  $d$  dimensions, the SCSA can be thought as the expansion in  $1/d$ . Here, we considered the subset of all non-crossing diagrams, which gives exact scaling in the limit of  $d \rightarrow \infty$ . The SCSA can be expressed diagrammatically as the following pair of coupled implicit equations



$$\text{Double line with square vertex} = \text{Single line with square vertex} + \text{Diagram with double line, square vertex, and dashed red loop}, \quad [14]$$



$$\text{Diagram with double line, square vertex, and dashed red loop with two arrows} = \text{Diagram with single line, square vertex, and dashed red loop with two arrows} + \text{Diagram with double line, square vertex, and dashed red loop with two arrows}, \quad [15]$$

where the double line represents the renormalized SCSA propagator  $\frac{1}{\kappa_R(q)q^4}$  and the solid circular vertex represents the renormalized SCSA vertex  $Y_R(q)$ . These equations can be solved self-consistently by considering the power-law scaling of the effective bending rigidity and the effective Young's modulus in the long wavelength limit, where it was found that

$$\frac{\kappa_R(q)}{\kappa} \sim \sqrt{\frac{Y h_v^2(q)}{\kappa}}, \quad \frac{Y_R(q)}{Y} \sim \sqrt{\frac{\kappa}{Y h_v^2(q)}}. \quad [16]$$

For the rippled  $Al_2O_3$  membranes in the experiments, the RMS height fluctuations scale with system size as  $h_v(q_0) \sim 1/q_0 \sim L$  according to Eq. (13), where  $q_0 = 2\pi/L$ . Therefore, the average effective bending rigidity scales with the system dimensions as

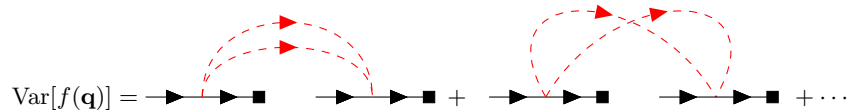
$$\frac{\kappa_R(q_0)}{\kappa_0} \sim \sqrt{\frac{Y_0 h_v^2(q_0)}{\kappa}} \sim \frac{h_v(q_0)}{t} \sim \frac{L}{t}. \quad [17]$$

### 3. Fluctuations in the effective bending rigidity

The theoretical analysis in the preceding sections can be extended to predict the scaling of sample-to-sample fluctuations in the effective bending rigidity in rippled membranes. As discussed in the previous section, mode coupling in Eq. (10) means that the applied normal force density of the form  $p(\mathbf{k}) = p_0 \delta_{\mathbf{k}, \mathbf{q}_0}$  also generates response  $f(\mathbf{x})$  that contains modes  $f(\mathbf{q} \neq \mathbf{q}_0)$ . However, upon considering the averaged quantity  $\text{Var}[f(\mathbf{q})] = \langle (f(\mathbf{q}) - \langle f(\mathbf{q}) \rangle)^2 \rangle$ , we find that  $\text{Var}[f(\mathbf{q})]$  is non-zero only for  $\mathbf{q} = \mathbf{q}_0$ . Thus, the variance of the linear response is related to the variance of the effective bending rigidity through

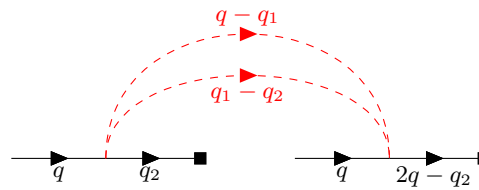
$$\text{Var}[f(\mathbf{q})] = \text{Var} \left[ \frac{1}{\kappa_R(q)} \right] \frac{p(\mathbf{q})^2}{q^8}. \quad [18]$$

In order to compute  $\text{Var}[f(\mathbf{q})]$ , a first attempt is to use iterative perturbation theory on Eq. (10). To the leading order, we find that



$$\text{Var}[f(\mathbf{q})] = \text{Diagram 1} + \text{Diagram 2} + \text{Diagram 3} + \dots \quad [19]$$

Upon using the diagrammatic rules from Eq. (10) and Eq. (11), the contributions of the two leading order diagrams to  $\text{Var}[f(\mathbf{q})]$  correspond to the following integral expressions:



$$\begin{aligned} &= \frac{1}{\kappa_0^2 q^8} \sum_{\mathbf{q}_1, \mathbf{q}_2 \neq 0} \frac{Y_0^2}{q_1^4 (q + q_1 - q_2)^4} |\mathbf{q} \times \mathbf{q}_1|^2 |\mathbf{q}_1 \times \mathbf{q}_2|^2 \\ &\quad \times |\mathbf{q} \times (\mathbf{q}_1 - \mathbf{q}_2)|^2 |(\mathbf{q} + \mathbf{q}_1 - \mathbf{q}_2) \times (2\mathbf{q} - \mathbf{q}_2)|^2 \\ &\quad \times \langle |h(\mathbf{q} - \mathbf{q}_1)|^2 \rangle \langle |h(\mathbf{q}_1 - \mathbf{q}_2)|^2 \rangle \frac{p(\mathbf{q}_2) p(2\mathbf{q} - \mathbf{q}_2)}{\kappa_0^2 q_2^4 (2q - q_2)^4}, \end{aligned} \quad [20]$$

$$\begin{aligned}
&= \frac{1}{\kappa_0^2 q^8} \sum_{\mathbf{q}_1, \mathbf{q}_2 \neq 0} \frac{Y_0^2}{q_1^4 (2q - q_1)^4} |\mathbf{q} \times \mathbf{q}_1|^4 |\mathbf{q}_1 \times \mathbf{q}_2|^2 |(2\mathbf{q} - \mathbf{q}_1) \times (2\mathbf{q} - \mathbf{q}_2)|^2 \\
&\quad \times \langle |h(\mathbf{q} - \mathbf{q}_1)|^2 \rangle \langle |h(\mathbf{q}_1 - \mathbf{q}_2)|^2 \rangle \frac{p(\mathbf{q}_2)p(2\mathbf{q} - \mathbf{q}_2)}{\kappa_0^2 q_2^4 (2q - q_2)^4}.
\end{aligned} \tag{21}$$

To facilitate the evaluation of the integrals, we use the ansatz  $p(\mathbf{k}) = p_0 \delta_{\mathbf{k}, \mathbf{q}_0}$ . From here on out, we also focus on the case of  $d_h > 2$ , which is applicable to the experiments, and we find that the diagrams in Eq. (20) and Eq. (21), up to a numerical prefactor, both give a contribution of the form

$$\frac{p_0^2 \delta_{\mathbf{q}, \mathbf{q}_0}}{\kappa_0^2 q^8} \frac{Y_0^2 \Delta^4}{\kappa_0^2 q^{2(d_h-1)} A} \sim \frac{p_0^2 \delta_{\mathbf{q}, \mathbf{q}_0}}{\kappa_0^2 q^8} \frac{Y_0^2 h_v^4(q)}{\kappa_0^2 q^2 A}, \tag{22}$$

where we used the expression for the RMS height fluctuations  $h_v(q)$  in Eq. (13). We also consider the higher order terms in the iterative series. As an example, we show one diagram that is part of the next order contribution to  $\text{Var}[f(\mathbf{q})]$  in iterative perturbation theory:

$$\begin{aligned}
&= \frac{1}{\kappa_0^2 q^8} \sum_{\mathbf{q}_1, \mathbf{q}_2, \mathbf{q}_3 \neq 0} \frac{(-Y_0^3)}{q_1^4 (q_1 - q_2 + q)^4 (q - q_1 + q_3)^4} |\mathbf{q} \times \mathbf{q}_1|^2 |\mathbf{q}_1 \times \mathbf{q}_2|^2 \\
&\quad \times |\mathbf{q} \times (\mathbf{q}_1 - \mathbf{q}_2)|^2 |(\mathbf{q}_1 - \mathbf{q}_2 + \mathbf{q}) \times \mathbf{q}_3|^2 \\
&\quad \times |\mathbf{q}_3 \times (\mathbf{q} - \mathbf{q}_1)|^2 |(\mathbf{q} - \mathbf{q}_1 + \mathbf{q}_3) \times (2\mathbf{q} - \mathbf{q}_2)|^2 \\
&\quad \times \langle |h(\mathbf{q} - \mathbf{q}_1)|^2 \rangle \langle |h(\mathbf{q}_1 - \mathbf{q}_2)|^2 \rangle \langle |h(\mathbf{q}_1 - \mathbf{q}_2 + \mathbf{q} - \mathbf{q}_3)|^2 \rangle \\
&\quad \times \frac{1}{\kappa_0 q_3^4} \frac{p(\mathbf{q}_2)p(2\mathbf{q} - \mathbf{q}_2)}{\kappa_0^2 q_2^4 (2q - q_2)^4} \\
&\sim \frac{p_0^2 \delta_{\mathbf{q}, \mathbf{q}_0}}{\kappa_0^2 q^8} \frac{Y_0^3 \Delta^6}{\kappa_0^3 q^{3d_h-4} A} \sim \frac{p_0^2 \delta_{\mathbf{q}, \mathbf{q}_0}}{\kappa_0^2 q^8} \frac{Y_0^3 h_v^6(q)}{\kappa_0^3 q^2 A}.
\end{aligned} \tag{23}$$

The upshot of evaluating these diagrams to identify that the variance of the response  $f(\mathbf{q})$  is a perturbative series in the parameter  $Y_0 h_v^2(q)/\kappa_0$ :

$$\text{Var}[f(\mathbf{q})] = \frac{p(\mathbf{q})^2}{\kappa_0^2 q^8} \frac{Y_0^2 h_v^4(q)}{\kappa_0^2 q^2 A} \left[ \alpha_0 + \alpha_1 \cdot \left( \frac{Y_0 h_v^2(q)}{\kappa_0} \right) + \dots \right], \tag{24}$$

where  $\alpha_i$  are numerical prefactors. Note that the parameter  $Y_0 h_v^2(q)/\kappa_0$  in the perturbation series is the same parameter that appears in the calculation for the average response  $\langle f(\mathbf{q}) \rangle$  discussed in the previous section. Thus, the iterative perturbation theory for  $\text{Var}[f(\mathbf{q})]$  also diverges in the long wavelength limit for the rippled  $Al_2O_3$  membranes in the experiments.

With the breakdown of perturbation theory, we can use the SCSA and sum all non-crossing diagrams to obtain an estimation for  $\text{Var}[f(\mathbf{q})]$  as:

$$\text{Var}[f(\mathbf{q})] = \Rightarrow \bullet \bullet \bullet \bullet \bullet \bullet + \Rightarrow \bullet \bullet \bullet \bullet \bullet \bullet + \Rightarrow \bullet \bullet \bullet \bullet \bullet \bullet + \dots, \tag{25}$$

where we recall that the double line represents the renormalized SCSA propagator  $\frac{1}{\kappa_R(q)q^4}$  and the solid circular vertex represents the renormalized SCSA vertex  $Y_R(q)$ . After focusing on the  $d_h > 2$  case of Eq. (13) that applies to the rippled  $Al_2O_3$  membranes in experiments, Eq. (16) gives us

$$\frac{\kappa_R(q)}{\kappa} \sim \sqrt{\frac{Y\Delta^2}{\kappa q^{d_h-2}}}, \quad \frac{Y_R(q)}{Y} \sim \sqrt{\frac{\kappa q^{d_h-2}}{Y\Delta^2}}. \quad [26]$$

We can determine how the contribution of the  $i$ -th diagram ( $i = 1, 2, \dots$ ) on the RHS of Eq. (25) scales with  $q$ . Upon taking  $p(\mathbf{k}) = p_0\delta_{\mathbf{k},\mathbf{q}_0}$ , the  $i$ -th diagram in the series above gives the contribution

$$\begin{aligned} \frac{p_0^2\delta_{\mathbf{q}_0,\mathbf{q}}}{\kappa_R(q)^2q^8} \sum_{\mathbf{q}_1,\dots,\mathbf{q}_{2i-1}\neq 0} & \left( \frac{Y_R(q_1)|\mathbf{q} \times \mathbf{q}_1|^2|\mathbf{q}_1 \times \mathbf{q}_2|^2}{\kappa_R(q)q^4q_1^4} \right)^2 \left( \frac{Y_R(q_3)|\mathbf{q}_2 \times \mathbf{q}_3|^2|\mathbf{q}_3 \times \mathbf{q}_4|^2}{\kappa_R(q_2)q_2^4q_3^4} \right)^2 \\ & \times \dots \left( \frac{Y_R(q_{2i-1})|\mathbf{q}_{2i-2} \times \mathbf{q}_{2i-1}|^2|\mathbf{q}_{2i-1} \times \mathbf{q}|^2}{\kappa_R(q_{2i-2})q_{2i-2}^4q_{2i-1}^4} \right)^2 \\ & \times \frac{\Delta^2}{A|\mathbf{q} - \mathbf{q}_1|^{d_h}} \frac{\Delta^2}{A|\mathbf{q}_1 - \mathbf{q}_2|^{d_h}} \dots \frac{\Delta^2}{A|\mathbf{q}_{2i-1} - \mathbf{q}|^{d_h}}, \end{aligned} \quad [27]$$

which, up to a numerical prefactor, goes as

$$\sim \frac{p_0^2\delta_{\mathbf{q}_0,\mathbf{q}}}{\kappa_0^2q^8} \cdot (q^2)^{2i-1} \cdot \left( \frac{\kappa_0q^{d_h-2}}{Y_0\Delta^2} \right)^{2i+1} \left( \frac{Y_0}{\kappa_0} \right)^{2i} \frac{\Delta^{4i}}{Aq^{2id_h}} = \frac{p_0^2\delta_{\mathbf{q}_0,\mathbf{q}}}{\kappa_0^2q^8} \left( \frac{\kappa_0q^{d_h-2}}{Y_0\Delta^2} \right) \frac{1}{Aq^2}. \quad [28]$$

Note that this result does not depend on  $i$ , so each diagram in the RHS of Eq. (25) gives a contribution that scales with  $q$  in the same way. Thus, the variance of the response  $f(\mathbf{q})$  to a body force  $p(\mathbf{q})$  goes as

$$\text{Var}[f(\mathbf{q})] \sim \frac{p(\mathbf{q})^2}{\kappa_0^2q^8} \left( \frac{\kappa_0q^{d_h-2}}{Y_0\Delta^2} \right) \frac{1}{Aq^2}. \quad [29]$$

Upon comparing to Eq. (18), we find that

$$\text{Var} \left[ \frac{\kappa_0}{\kappa_R(q)} \right] \sim \frac{\kappa_0q^{d_h-4}}{Y_0\Delta^2A}, \quad [30]$$

and this can be used to estimate  $\text{Var} \left[ \frac{\kappa_R(q)}{\kappa_0} \right]$ . For a random variable  $x$  with mean  $\bar{x}$ , the variance of  $f(x)$  can be approximated by  $\text{Var}[f(x)] \approx [f'(\bar{x})]^2 \text{Var}[x]$ . If  $f(x) = 1/x$ , then  $\text{Var}[1/x] \approx \text{Var}[x]/\bar{x}^4$ . Thus, we obtain

$$\text{Var} \left[ \frac{\kappa_R(q)}{\kappa_0} \right] \sim \frac{Y_0\Delta^2}{\kappa_0Aq^{d_h}} \sim \frac{Y_0h_v^2(q)}{\kappa_0Aq^2}. \quad [31]$$

By considering the rippled  $Al_2O_3$  membranes in experiments with  $d_h = 4$  of size  $L \times L$ , the standard deviation of the effective bending rigidity at the scale of the system ( $q \sim 1/L$ ) scales as

$$\text{Std} \left[ \frac{\kappa_R(L)}{\kappa_0} \right] \sim \sqrt{\frac{Y_0h_v^2(L)}{\kappa_0}} \sim \frac{L}{t}. \quad [32]$$

Since the average effective bending rigidity also scales as

$$\text{Avg} \left[ \frac{\kappa_R(L)}{\kappa_0} \right] \sim \frac{L}{t} \quad [33]$$

as shown in Eq. (17) in the previous section, this means that the ratio  $\text{Std}[\kappa_R(L)]/\text{Avg}[\kappa_R(L)]$  remains finite at large scales. Therefore, the effective bending rigidity of rippled  $Al_2O_3$  is not self-averaging.

#### 4. Buckling in rippled membranes

In this section, we discuss how frozen ripples affect the buckling of a rippled sheet in response to uniaxial compression. As the ripples lead to an effective stiffening of the bending rigidity and softening of the Young's modulus, rippled sheets have an increased buckling threshold compared to smooth sheets. In the main text, a kirigami structure was fabricated from a rippled membrane. The resulting rippled metamaterial (of thickness  $t$ ) has triangular domains of size  $L_d$  and hinges of size  $L_h$ . The mechanical response to an extensional force on the structure changes from a regime where the triangular domains rotate in-plane to a regime where the domains rotate out-of-plane due to buckling in the hinges.

Thus, it is useful to consider how ripples affect buckling in a  $L_h \times L_h$  hinge with thickness  $t$ . First, let us consider a smooth hinge. The critical uniaxial compressive strain for buckling a smooth hinge out of plane is

$$\epsilon_c \sim \frac{\kappa_{1D}}{Y_{1D}} \cdot q_0^2, \quad [34]$$

where  $q_0 \sim 1/L_h$  is the longest wavelength mode. From the beam theory, we know that the bending rigidity scales as  $\kappa_{1D} \sim EL_h t^3$  and the 1D Young's modulus scales as  $Y_{1D} \sim EL_h t$ , where  $E$  is the 3D Young's modulus. This gives the scaling for the critical compressive strain

$$\epsilon_c \sim \left(\frac{t}{L_h}\right)^2. \quad [35]$$

Let us now consider the case of kirigami cuts in a rippled sheet. We can estimate the buckling threshold for a rippled hinge by

$$\epsilon_c^{(R)} \sim \frac{\kappa_{1D}^{(R)}}{Y_{1D}^{(R)}} \cdot q_0^2, \quad [36]$$

and so

$$\frac{\epsilon_c^{(R)}}{\epsilon_c} \sim \frac{\kappa_{1D}^{(R)}/\kappa_{1D}}{Y_{1D}^{(R)}/Y_{1D}}. \quad [37]$$

Upon taking

$$\frac{\kappa_{1D}^{(R)}}{\kappa_{1D}} \sim \frac{h_v}{t} \quad \text{and} \quad \frac{Y_{1D}^{(R)}}{Y_{1D}} \sim \frac{t}{h_v}, \quad [38]$$

where  $h_v$  corresponds to the RMS height fluctuations over the  $L_h \times L_h$  hinge, we get

$$\epsilon_c^{(R)} \sim \left(\frac{h_v}{t}\right)^2 \epsilon_c \sim \left(\frac{L_h}{t}\right)^2 \epsilon_c \sim \left(\frac{h_v}{L_h}\right)^2. \quad [39]$$

This result has an intuitive interpretation, as  $h_v$  is the effective thickness of the rippled hinge, and the critical compressive strain for buckling of a rippled hinge is increased compared to a smooth hinge.

## 5. Effective temperature

In this section, we estimate the effective temperature needed to generate height fluctuations in a flat sheet that are comparable to the quenched random height disorder seen in the experimental samples. Thermal fluctuations of a flat sheet lead to height fluctuations of the form

$$\langle |h(\mathbf{q})|^2 \rangle \approx \frac{k_B T}{A \kappa_0 q^4}, \quad [40]$$

where the sample area is  $A = 284 \times 213 \mu\text{m}^2$  and the bending rigidity of 28 nm thick aluminum oxide is  $\kappa_0 \approx 0.34$  pJ. Using the PSD data from Fig. 1b of the main text, we can estimate

$$T_{\text{backside}} \sim 10^{10} \text{ K} \quad \text{and} \quad T_{\text{frontside}} \sim 10^4 \text{ K}. \quad [41]$$

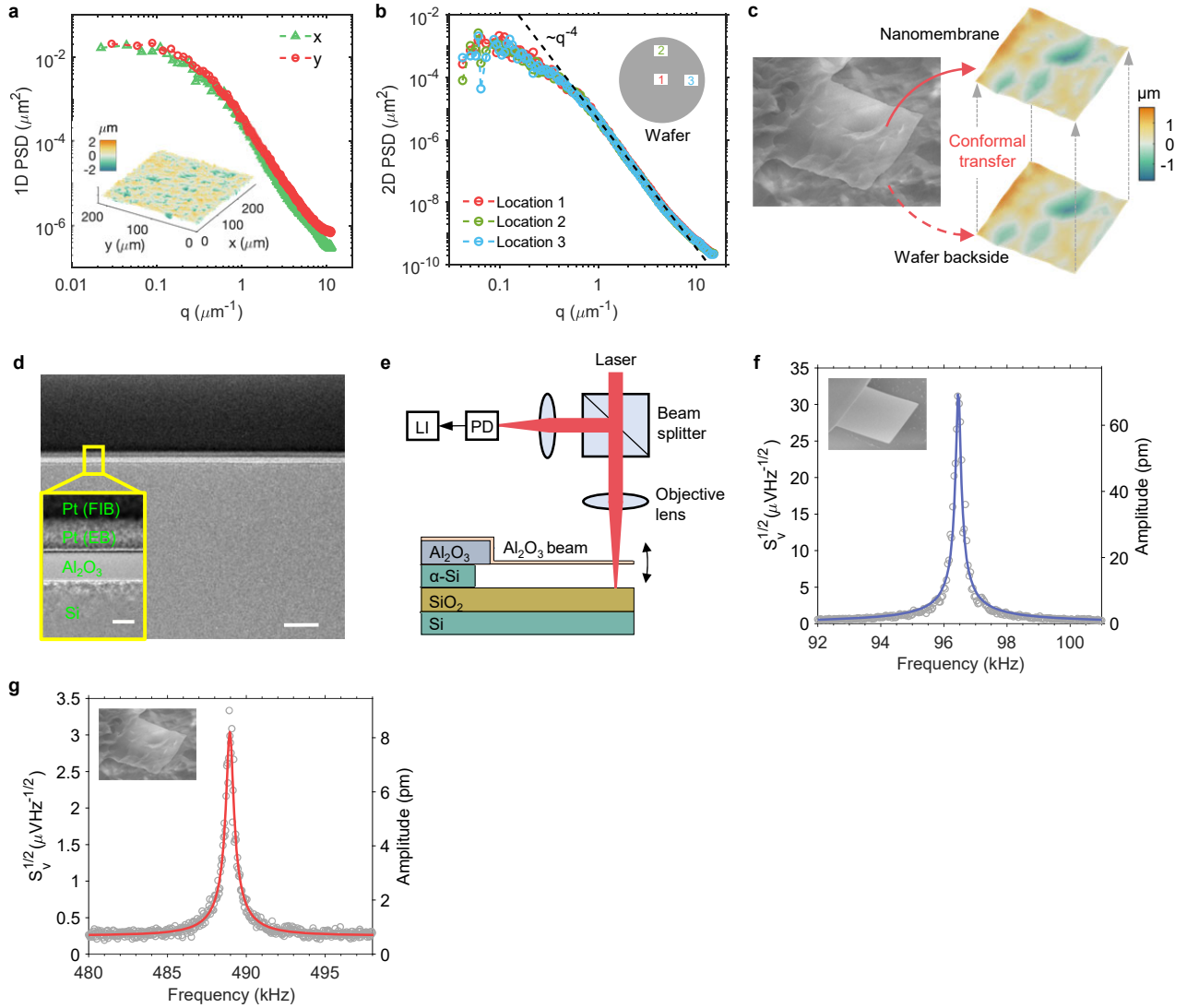


**Fig. S1. Characterization and measurement** **a**, 1D PSD of the wafer backside surface height profile  $P(\mathbf{q}) \equiv |h(\mathbf{q})|^2$  measured with a confocal microscope, where the  $x$  and  $y$  directions correspond to the wavevectors  $(q_x, 0)$  and  $(0, q_y)$ , respectively. The insert shows the confocal microscopy image, measured over an area of  $284 \times 213 \mu\text{m}^2$ . **b**, The 2D PSD of the wafer backside surface height profiles, measured over an area of  $284 \times 213 \mu\text{m}^2$  at multiple locations, as illustrated in the inset figure. **c**, Conformal transfer approach for controllable freezing of the substrate morphology to the nanomembrane. The confocal microscopic images show the measured morphologies of the rippled nanomembrane and the underneath wafer surface, respectively. **d**, Cross-sectional scanning transmission electron microscopy (STEM) image shows a  $t = 28$  nm-thick  $\text{Al}_2\text{O}_3$  nanofilm deposited on the frontside of a wafer surface, scale bar  $0.5 \mu\text{m}$ . Scale bar for the insert image is  $20$  nm. The electron beam (EB) and focused ion beam (FIB)  $Pt$  films are protective layers for STEM sample preparation. **e**, Schematic diagram of the optical interferometry setup. The optical interference between the nanobeam and the underneath substrate is detected by a photodetector (PD) and analyzed by a lock-in amplifier (LI). **f-g**, Thermomechanical motion spectra of a smooth (**f**) and a rough (**g**) nanomechanical resonator measured with optical interferometry. SEM images of the smooth and rough resonator are shown as insert ( $L = W = 20 \mu\text{m}$ ,  $t = 28$  nm). Solid lines show the curve fittings to the Lorentzian function for harmonic resonators.

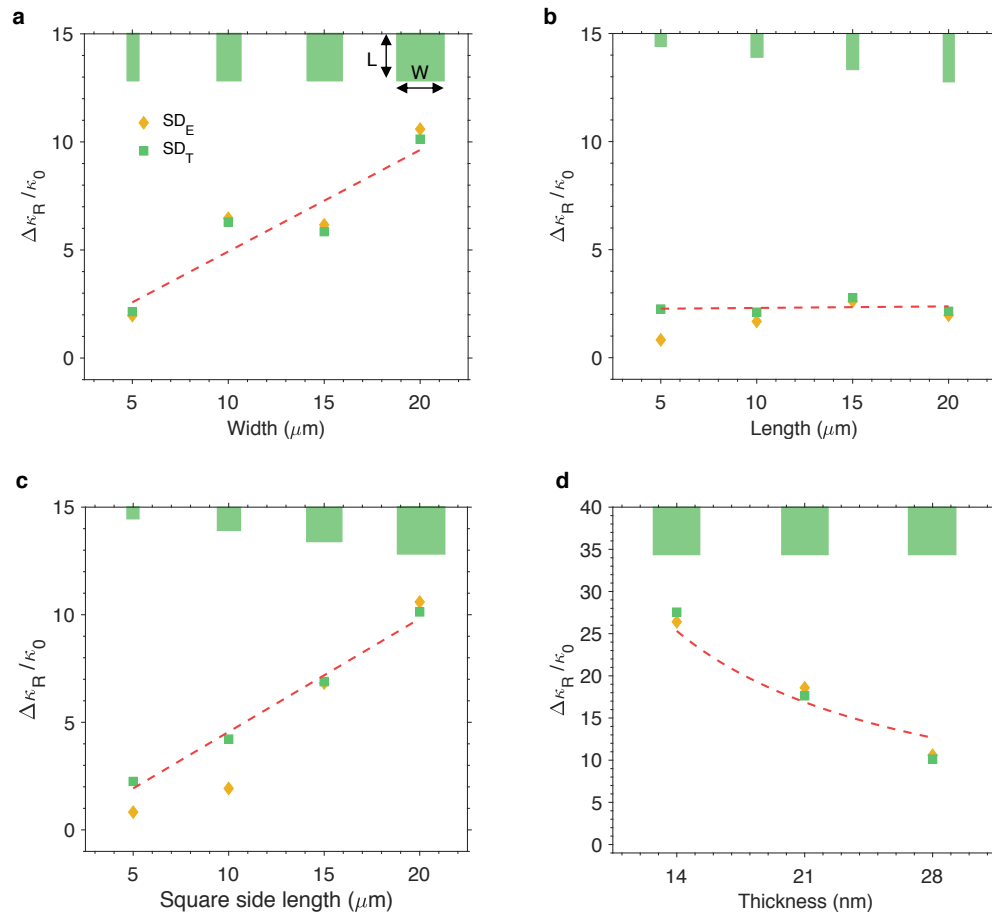


**Fig. S2. Scale-dependent standard deviation of the effective bending rigidity of rippled nanomembranes.** **a-d**, Standard deviation of the effective bending rigidity  $\kappa_R$  of rippled cantilevers as a function of the sample dimensions: **a**, variable width  $W$  ( $L = 20 \mu\text{m}$ ,  $t = 28 \text{ nm}$ ), **b**, variable length  $L$  ( $W = 5 \mu\text{m}$ ,  $t = 28 \text{ nm}$ ), **c**, variable side length  $L = W$  of square cantilevers ( $t = 28 \text{ nm}$ ), and **d**, variable thickness  $t$  ( $L = W = 20 \mu\text{m}$ ). The standard deviations  $\Delta\kappa_R$  are estimated using the relation  $\Delta\kappa_R = \sqrt{\sum_{i=1}^n (\kappa_i - \bar{\kappa}_R)^2 / n}$ , where  $\kappa_i$  is a measured effective bending rigidity of sample  $i$ ,  $n$  is the total number of samples, and  $\bar{\kappa}_R$  is the mean value of the effective bending rigidity. Plotted are the standard deviations for experimental data, where the average value  $\bar{\kappa}_R$  was either obtained experimentally ( $\text{SD}_E$ ) or via theoretical predictions ( $\text{SD}_T$ ). The dashed lines show the fitting to the predicted theoretical scaling  $\Delta\kappa_R/\kappa_0 \sim W/t$ .



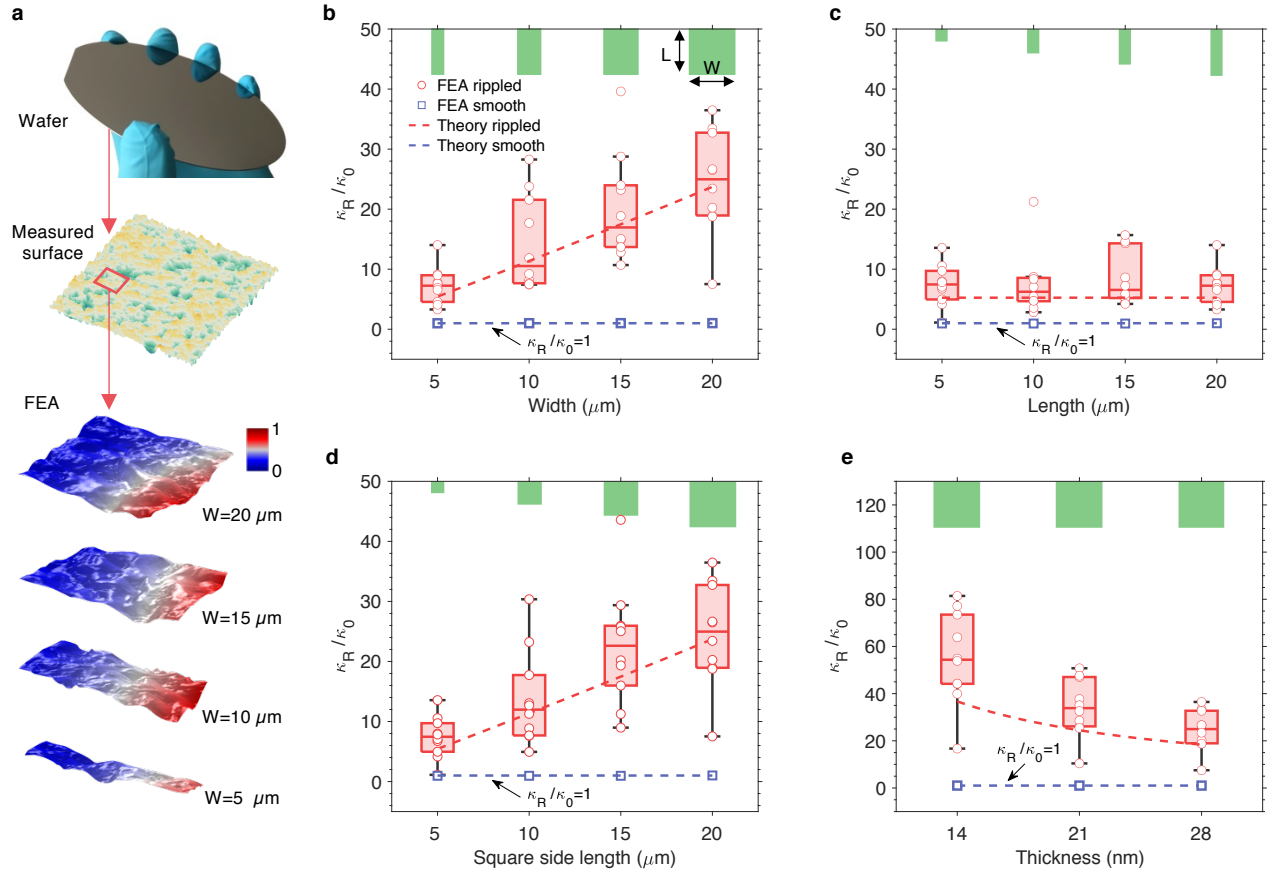


**Fig. S3. Finite element analysis (FEA) of the effective bending rigidity of rippled nanomembranes.** **a**, Illustration of FEA processes. The fundamental vibration mode shapes (out-of-plane bending) of disordered  $Al_2O_3$  nanocantilevers ( $L = 20 \mu\text{m}$ ,  $t = 28 \text{ nm}$ ) with different widths  $W$  are shown, where the color bar represents the normalized amplitude of the out-of-plane bending. **b-e**, FEA results for the effective bending rigidity  $\kappa_R$  of smooth and rippled cantilevers as a function of the sample dimensions: **b**, variable width  $W$  ( $L = 20 \mu\text{m}$ ,  $t = 28 \text{ nm}$ ), **c**, variable length  $L$  ( $W = 5 \mu\text{m}$ ,  $t = 28 \text{ nm}$ ), **d**, variable side length  $L = W$  of square cantilevers ( $t = 28 \text{ nm}$ ), and **e**, variable thickness  $t$  ( $L = W = 20 \mu\text{m}$ ). The effective bending rigidity  $\kappa_R$  is obtained from the resonant frequency of the cantilever (see text) and compared to the bending rigidity  $\kappa_0 = Et^3/12(1-\nu^2)$  of flat nanofilms ( $\kappa_0 = 0.34 \mu\text{J}$  for  $t = 28 \text{ nm}$ -thick  $Al_2O_3$  films with the Young's modulus  $E = 180 \text{ GPa}$  and Poisson's ratio  $\nu \approx 0.2$ ). The green insert in each figure shows the relative planar dimensions of cantilevers. Each box plot contains 10 samples of same dimension, where the box encompasses 25<sup>th</sup> to 75<sup>th</sup> percentiles, the centre line shows the median and whiskers extend to the minimum and maximum values ( $\pm 2.7 \text{ SD}$ ) not considered outliers. The dash lines are the theoretical scaling prediction (see text). Plots in **c-e** have the same legend as the plot in **b**.

**Movie S1. Rippled elastic metamaterial with delayed buckling. The millimeter-scale kirigami structure, created by cuts on a 28-nm-thick rippled  $Al_2O_3$  elastic thin sheet, deforms under a uniaxial force applied using a nanoprobe manipulator.**

## References

1. Košmrlj, Andrej, and David R. Nelson. "Mechanical properties of warped membranes." *Physical Review E* 88, no. 1 (2013): 012136.
2. Košmrlj, Andrej, and David R. Nelson. "Thermal excitations of warped membranes." *Physical Review E* 89, no. 2 (2014): 022126.
3. Bray, Alan J. "Self-consistent screening calculation of the critical exponent  $\eta$ ." *Physical Review Letters* 32, no. 25 (1974): 1413.
4. Bray, Alan J. "Statistical mechanics of zero-dimensional ginzburglandau fields: Accuracy of the screening approximation." *Journal of Statistical Physics* 11 (1974): 29-50.
5. Le Doussal, Pierre, and Leo Radzihovsky. "Self-consistent theory of polymerized membranes." *Physical Review Letters* 69, no. 8 (1992): 1209.
6. Gazit, Doron. "Structure of physical crystalline membranes within the self-consistent screening approximation." *Physical Review E* 80, no. 4 (2009): 041117.
7. Zakharchenko, K. V., R. Roldán, A. Fasolino, and M. I. Katsnelson. "Self-consistent screening approximation for flexible membranes: Application to graphene." *Physical Review B* 82, no. 12 (2010): 125435.
8. Radzihovsky, Leo, and Pierre Le Doussal. "Crumpled glass phase of randomly polymerized membranes in the large  $d$  limit." *Journal de Physique I* 2, no. 5 (1992): 599-613.
9. Le Doussal, Pierre, and Leo Radzihovsky. "Flat glassy phases and wrinkling of polymerized membranes with long-range disorder." *Physical Review B* 48, no. 5 (1993): 3548.